Free Energy of a Polymer in Slit-Like Confinement from the Odijk Regime to the Bulk: Supporting Information

Jason S. Leith,[†,§] Albert Kamanzi,[†,§] David Sean,[‡] Daniel Berard,[†] Andrew C. Guthrie ,[†] Christopher M. J. McFaul,[†] Gary W. Slater,[‡] Hendrick W. de Haan,[*,¶] and Sabrina R. Leslie[*,†]

†*McGill University, Montreal, Quebec, Canada*

‡*University of Ottawa, Ottawa, Ontario, Canada*

¶*University of Ontario, Institute of Technology, Oshawa, Ontario, Canada*

§*These authors contributed equally to this work.*

E-mail: hendrick.dehaan@uoit.ca; sabrina.leslie@mcgill.ca

Methods

Flow cell preparation

Standard coverslips, No. 1 (25-mm square, 130–150-μm thick, part No. 48366-089, VWR) and No. 1.5 (25-mm square, 160–190-μm thick, part No. 48366-249, VWR), were used to make the imaging flow cells. The No. 1 coverslips were UV-laser-etched to form sample inlets. Coverslips were cleaned by immersing them in a warm bath of Hellmanex III detergent, followed by ethanol, acetone, and then deionized water baths, consecutively, all at 50°C for 20 minutes each. They were then treated with piranha solution (2:1 mixture of sulfuric acid

and 30% hydrogen peroxide) for 30 minutes and finally with 1M potassium hydroxide for 15 minutes.

Flow cells were formed by adhering the No. 1.5 coverslips to the No. 1 coverslips using a double-sided adhesive tape (30-μm thick, Nitto Denko 5603; 10-μm, Nitto Denko 5601). Tape patterns were laser-cut at the center to form a flow channel and a circular imaging chamber, as shown in Figs. 1b and 4 of Berard *et al.*[1] The choice of tape thickness determines the height gradient of the chamber.

DNA sample preparation:

Linearized pUC19 samples were extracted and purified from transfected E. coli cells and then treated with the single-cutting restriction endonuclease NdeI (NEB), and purified on a spin column (Qiagen) into in a 1× TE buffer solution (10 mM tris-Cl (pH 8.0) and 1 mM EDTA). EDTA was added to chelate divalent cations to inhibit DNase activity from enzymatic contaminants.

DNA labeling was done by preparing equal volumes of the DNA sample in 1× TE buffer and YOYO-1 dye (absorption peak = 489 nm), also dissolved in 1× TE. The YOYO-1 concentration was set such that there were 10 base pairs per YOYO-1 molecule. As YOYO-1 lengthens dsDNA by 0.5 nm per YOYO-1 molecule, for our pUC19 plasmid of 2686 bp, the contour length increases by 134 nm, to 1.047 μm,[2] corresponding to an ideal wormlike-chain R_g in bulk of 123 nm. The DNA was added to the YOYO-1 and left to sit in the dark for 50 minutes. The sample was then refrigerated, ready for experiments.

Nonreactive Cy5 dye (absorption peak = 650 nm) was used for chamber height measurements. It was also prepared in 1× TE buffer and refrigerated.

Immediately before performing experiments, the labeled DNA and Cy5 were added to the experimental buffer, 50 mM tris-Cl (pH 8.0), 1 mM EDTA, along with 1:100 β-mercaptoethanol (BME) as an anti-photobleaching agent. The BME also prevents photon-icking of the DNA caused by covalent reactions between the DNA and YOYO-1 dye. At pH

8.0 at room temperature, tris is 64% ionized and EDTA is mostly triply ionized, and so the ionic strength of our solution was 35 mM, which gives a Debye length < 2 nm, so the DNA's electrostatic interaction with the walls is negligible. Also, at this ionic strength, the Kuhn length has been predicted by OSF theory to deviate negligibly from the standard value of 100 nm.[3,4] Competing theories exist,[5,6] but experimental measurements are in insufficient agreement to conclusively support any one over another,[7,8] and so we have elected to assume L_K =100 nm.

Microscope and illumination

The experiments were performed on a Nikon TI-E microscope with a 60× NA 1.49 oil immersion objective (Nikon part no. MBH76160) or a 40× NA 1.30 oil immersion objective (Nikon part no. MRH01401). The objective was mounted on a Perfect Focus System (PFS), which allows for automated corrections of drift in the objective's focus. Images were acquired with an Andor iXon 897 EMCCD camera with the sensor cooled to −70°C. A Coherent 488-nm Sapphire laser was used to excite stained DNA molecules, with its power 3.6–7.2mW at the objective, and 50-ms exposure time. The same 488-nm laser was used to acquire interference fringe images, attenuated to 0.036–0.072 mW at the objective with an OD2 neutral density filter, for chamber geometry characterization. A second laser (647-nm Coherent OBIS at approximately 0.1 mW power) was used to acquire dye images, also to be used for chamber geometry characterization.

CLiC microscopy setup

The prepared flow cell was placed on a microscope plate. A chuck shown in Fig. 1 (main text), with reservoirs for flowing samples into the flow cell was mounted onto the flow cell and microscope plate, using thumbscrews. The microscope plate was then mounted on an XY-meso stage (Mad City, custom-made) above the objective of the microscope.

The flow cell chamber was initially wetted with 50-mM tris-Cl (pH 8.0), 1-mM EDTA

solution. The push-lens was then lowered (controlled by a nano-positioner, part No. P-602.1SL, Physik Instrumente) onto the flow cell to form the CLiC chamber. The distance required to achieve coverslip-coverslip contact was determined by observing interferometry rings. To establish a stable imaging chamber, the push-lens was over-pushed by 2 μm beyond the first point of contact. Measurements were done by performing raster scans (with grids of 15×15 to 21×21 fields of view, see Fig. S1). Chamber stability and symmetry were verified before flowing in DNA samples. Typically, the chamber stabilized completely after tens of minutes, but three fringe scans (Fig. S1a) were taken over a period of one hour to be certain.

Once a stable chamber was verified (by reproducible fringe profiles), the DNA sample was prepared for flowing into the imaging chamber. DNA samples were diluted to a desired concentration, mixed with the Cy5 dye (final concentration, 2.3 μM), and loaded into the chamber. This concentration of DNA in the chamber, denoted as the bulk concentration C_{bulk}, determined the accessible range of confinement height. Hence several experiments with varying C_{bulk} were performed as shown in Fig. 2 (main text).

Data collection

The DNA sample was allowed to equilibrate for an hour after insertion into the chamber. This period was established by repeatedly measuring concentration profiles after this elapsed time and identifying when concentration as a function of position stopped varying with time. Data collection involved a sequence of measurements of the dye scans (Fig. S1b), DNA scans (Fig. S2), and fringe scans (Fig. S1a), taken in that order. There was no risk from the dye scan of bleaching the DNA, since YOYO-1's absorption at 647 nm and Cy5's absorption at 488 nm are both negligible. Interferometry scans were performed after the first DNA scan since they were performed with the same laser wavelength as the DNA scan. Additionally, the laser intensity was decreased by a factor of 100 when performing fringe scans.

Both the DNA and the dye scans required acquiring high resolution images (80-μm square field of view). The PFS was used to adjust the focus during scans to correct for small

deformations in the bottom of the chamber when required (∼100 nm or less, for the entire imaged region). Measurements were repeated over several hours, to verify chamber geometry stability and sample equilibration. Once enough measurements were obtained, the push-lens was lifted such that the chamber was ~ 0.5 μm at the center. A dye fluorescence image was taken at this height, denoted the "probe image", to capture the spatial variation in the illumination intensity.

Data analysis

Chamber height characterization

Chamber height calculations were performed in Matlab. Characterizing chamber geometry was performed in two steps. First, dye fluorescence intensity throughout the chamber (which is proportional to chamber height) was fitted to a sixth-order, two-dimensional polynomial. Second, direct interferometry was performed as described by Berard *et al.*[1] Interferometry data was used to scale and constrain the chamber fit based on the dye fluorescence.

Images taken of dye fluorescence were first normalized by a Gaussian fit of the probe image. This was necessary to eliminate the laser beam profile, which gives a noticeable rasterization effect, from the dye fluorescence images. The normalization was done as shown below;

$$I_{\text{norm}} = \frac{I_{\text{scan}} - \min(I_{\text{scan}})}{\tilde{I}_{\text{probe}} - \min(\tilde{I}_{\text{probe}})} + \min(I_{\text{scan}}) \tag{1}$$

where I_{scan} are the scan images, $\min(I_{\text{scan}})$ and $\min(\tilde{I}_{\text{probe}})$ are the minimum intensity pixel of all the scan and probe images, respectively, and $\tilde{I}_{\text{probe}}$ is the Gaussian fit of the probe image.

The normalized dye images were stitched into a single image—a *dye scan*, as shown in Fig. S1b. To reduce rasterization effects, the edges of the fields of view making up the

complete dye scan were masked out (Fig. S1c). The stitched image was then fitted to a sixth-order polynomial subject to constraints (discussed below). Residuals between the fit and the rasterization-corrected dye scan are shown in Fig. S1g,h. The fitting relied on the coverslip-coverslip contact during measurements. This was achieved in experiments by over-pushing the push-lens (as mentioned in CLiC Microscopy setup above) and monitoring the interferometry scans, making sure the center remained maximally dark.

The interferometry images, Fig. S1a, were used determine the fitted chamber height map in two ways. First, they were use to constrain the polynomial fit of the stitched dye scan. Pairs of points on different fringe minima (dark rings) i and j were chosen and the fit at those points was required to yield a ratio of $i/j \pm 0.02$ at these positions. Chamber heights at interferometry minima were given by

$$h_m = \frac{m\lambda}{2n}\frac{1}{\cos(\theta)} \tag{2}$$

where m is the mth dark ring from the center, λ is the illuminating laser's wavelength, n is the solution's index of refraction, and θ is the laser beam's incident angle.

In addition to constraining the fit algorithm, the fringe minima were used to scale the resulting polynomial fit, converting it from intensity units to nanometers. The fit was scaled by fixing the height at a fringe minimum as close to the middle of the dataset's usable height range to the height given by Fig. 2 and the height at the minimum of the polynomial fit to zero. Fig. S1c shows a profile of the dye fitting along a vertical axis, and it agrees with the interferometry rings. Height assignments are accurate within 5% based on systematic and statistical uncertainty in the chamber height fit, as described in Ref.[1,9] and in Fig. S1, except at heights < 100 nm. Here, near the point of coverslip-coverslip contact, the chamber geometry is distorted from a polynomial. At these low heights, we find that scaling the fit using the two innermost interferometry minima rather than fixing the minimum of the fit to zero height gives better results (Fig. S3). The effect of this alternative scaling procedure

is significant only for the two highest-concentration data sets, $C_{\mathrm{bulk}}/\max(C_{\mathrm{bulk}}) = 1.0$. For datasets with all heights > 100 nm, the difference between the two methods of scaling the polynomial fit is negligible.

Horizontal error bars in Fig. 3 of the main text were assigned as follows. Within each annulus representing a height bin, the height at every pixel is determined directly from dye fluorescence (converted from intensity to nanometers using the interferometry scan). As the dye scan has experimental noise and a non-constant excitation profile, the range of heights as would be implied by the dye scan within an annulus is greater than the range of heights in the polynomial fit within the same annulus. The horizontal error bars indicate the range from the 25th to the 75th percentile in these dye-derived heights (rather than the fit-derived heights).

Particle identification and trajectory analysis

This step was performed using an ImageJ plugin that we adapted for our purposes for particle detection and tracking. It uses the "feature point detection and tracking algorithm" as described by Sbalzarini and Koumoutsakos.[10] Mobile particles were consistently $5 \sim 10$ times brighter than the noise floor, and of visually uniform brightness. After the tracking algorithm was run, resulting trajectories were inspected to ensure that the tracker accurately found particles.

Before executing the particle-tracking algorithm, regions of interest were selected for each dataset. The highest trackable height was limited by either DNA's bulk concentration or the objective's depth of focus (Fig. S2c top image). The lowest trackable region is also limited by bulk concentration and particles exclusion. Areas of the scan with heights outside this trackable regime were masked out, as shown in Fig. S2b.

Counting particles as a function of height

Every trajectory was assigned to a chamber-height bin (determined from its x, y coordinates and the aforementioned height map). During a movie, particles can enter or exit a field of view or visually overlap with other particles and thus create trajectories shorter in duration than that of the movie. Accordingly, we multiplied each trajectory's contribution to the total particle count of a bin by the fraction of the movie for which the trajectory is found in the bin. This produces *notional* particle count $N(h)$ shown in Fig. 2a (main text) as a function of height for a series of different bulk concentrations C_{bulk}.

$$N_{\text{average}}(h) = \frac{\sum_{i}^{N} t_i}{T \cdot A_{\text{annulus}}} \tag{3}$$

where $N_{\text{average}}(h)$ is the particle concentration in one of the binned annulus at height h, N is the number of trajectories in the bin, t_i is the length of time of the ith trajectory, T is total length of the movie, and A_{annulus} is the annulus area.

In regions of high areal concentration, particles frequently visually collide, and the tracking algorithm momentarily loses a particle. This can result in an undercounting of lifetime-weighted particles. To ensure that our analysis was not significantly affected by this undercounting, we performed simulations of particles undergoing normal diffusion. Movies of this simulated data were constructed using experimentally determined point-spread-functions of the particles and experimental noise. We found that at an areal density of 10^{-8} particles per nm^2, 2% of total trajectory length is lost, and so for all datasets, only height annuli with areal densities below this value were included. Undercounting can also be caused by particles momentarily moving outside of the depth of focus of the optical system, although at heights and concentrations used in our work this effect is less prevalent than undercounting due to particle overlap.

Calculating the confinement potential

The confinement potential calculations were performed using the relation for the change in free energy as a function of concentration.

$$C(h) = C_{\text{bulk}} \exp\left[\frac{-\triangle G_{\text{conf}}(h)}{k_{\text{B}}T}\right] \tag{4}$$

$$\frac{\triangle G_{\text{conf}}(h)}{k_{\text{B}}T} = -\ln\left[\frac{N_{\text{average}}(h)}{h}\right] + \ln(C_{\text{bulk}}) \tag{5}$$

where $C(h)$ is the particle concentration at height h, and $\triangle G_{\text{conf}}$ is the change in confinement free energy.

For each height h, a weighted mean of the ΔG_{conf} values from all datasets that were analyzed at that height was computed. Weights were proportional to the total number of particles counted for that height in a dataset.

Assigning bulk concentration per dataset

A direct endogenous determination of the true bulk concentration C_{bulk} of a DNA in a dataset cannot be made in the experimental chamber. C_{bulk} may differ from the concentration based on spectrophotometic measurements of stock solution and dilution ratios because of (1) aggregation, (2) fragmentation of DNA, (3) the sticking of molecules to apparatus surfaces, and (4) inaccuracy of pipettes used for dilution. As (1–3) can only reduce the true C_{bulk}, we expect it to be lower than the calculated concentration in the sample tube, C_{tube}.

To identify the true concentration of DNA in our experiments, we followed a two-step procedure. The first step is to measure the relative concentration at common heights across experiments to scale one experiment to another. We counted the number of particles in the highest common height annulus* for the highest-concentration datasets ($C_{\text{bulk}}/\max(C_{\text{bulk}}) =$

*The highest annulus in a particular experiment is the binning at the highest height in that experiment. For a set of experiments with overlapping heights, the highest common annulus is the binning at the highest

1.0 in Fig. 2 (main text)). We then scaled C_{tube} of lower-concentration datasets ($0.1 < C_{\text{bulk}}/\max(C_{\text{bulk}}) < 1.0$) that overlapped with this annulus so that the resulting concentrations of the lower-concentration datasets would imply the observed number of particles in the annulus[†]. We repeated this procedure for the next set of lower-concentration datasets, adjusting their nominal concentrations based on the highest common annulus of the preceding set. These adjustments to C_{tube} were determined entirely by the observed concentrations of particles at overlapping annuli, and used no fitted or free parameters.

After this adjustment of concentration ensured that the datasets were internally consistent, we fitted the average ΔG_{conf} curve resulting from the 16 datasets to a combined theory curve. For the purpose of this fit, the prefactor in the Casassa formula is adjusted to take into account the semiflexibility of our polymers (see SI, "Simulations"); the prefactor is the unique choice that positions the Casassa curve such that there is a single point at which it agrees with the CS curve in both free energy and force of confinement. Geometrically this is equivalent to moving the Casassa curve vertically on a log-log plot until it is tangent to the CS curve.

The combined theory curve is defined by the Chen-Sullivan (CS) curve at heights lower than the height at which the CS and Casassa curves coincide and by the Casassa curve at greater heights (see Fig. 3 (main text). We fit for a single parameter by which to multiply every dataset's adjusted C_{bulk} that minimized the sum-of-squares difference between the theory curve and the mean ΔG_{conf}. It is important to fit the mean ΔG_{conf} data rather than measurements of ΔG_{conf} from each individual dataset so as not to bias the fit toward height regions that happen to be dense with experiments. The value of this parameter was 0.86, reflecting a reduction of 14% in the true C_{bulk} relative to the endogenously-rescaled C_{tube} values.

shared height.

[†]The goal of this step is to estimate the true concentration of each experiment. The experiments at the lowest heights used higher nominal concentrations; and hence required less dilution and pipetting, introducing less potential for error. We therefore chose them to estimate the bulk concentration of those experiments that used lower concentrations and had overlapping heights.

Simulations

In order to map out the free energy from the bulk to Odijk scaling regimes, two simulation approaches are used: a Monte Carlo (MC) method is used for larger slit heights and Langevin Dynamics (LD) simulations are performed for very tight slits.

For the Monte Carlo simulations, persistent pseudorandom walks are built by picking a random displacement unit vector $\vec{v}_n$ and evaluating its associated energy

$$U_{\text{bend}} = \kappa \left(1 - \cos\theta\right), \tag{6}$$

in relation to the previous bond vector $\vec{v}_{n-1}$. The step is rejected or accepted using a Metropolis scheme. To calibrate the model, unconfined chains of N-steps between 10–1000 are built in free space. From those conformations, the effective persistence length is found by a fit to the Kratky-Porod relation. We find that $\kappa = 5.0$ yields chains with a persistence length of $L_{\text{p}} \approx 4.0$ unit bond vectors. From this, our MC chain consists of $N = 84$ steps which corresponds to the persistence-length–to–contour-length ratio of pUC19.

The MC approach is then used to generate an ensemble of conformations for a given slit height. The walk is initiated by randomly placing the first monomer between the confining walls. We assume a uniform distribution for the chain ends between the walls. Additional monomers are added via the scheme outlined above. If the chain crosses one of the two walls, the growth of that chain is terminated — this is counted as a disallowed conformation. Conversely, an allowed conformation is generated when all N steps are made with no disallowed moves.

As the size of the ensemble grows, the ratio of the allowed to total (allowed + disallowed) conformations approaches the ratio of the partition functions for confined to unconfined chains which leads to a direct calculation of the confinement free energy. For wall spacings of h between 5–2000, we use $N_{\text{try}} = 1 \times 10^8$ attempts but need to increase it for wall spacings of $h = 2$, 3, and 4 unit bond vectors in order to obtain sufficient successful attempts.

To investigate the effect of semiflexibility, these calculations were performed for polymers of varying persistence lengths, $\kappa = (0, 5, 10, 20)$, and lengths, $N = (50, 100, 200, 500)$. From these results, we find that the Casassa formula (Eq. 4 of main text) contains a model-dependent prefactor, even considering its effect on R_g. The free-energy cost of semi-flexible chains decreases from the value predicted by Casassa's formula for a flexible chain as chain rigidity increases, reflecting the fact that a semi-flexible chain contains a diminished number of degrees of freedom and thus has fewer conformations eliminated by the walls. We find that this effect can be absorbed into a stiffness-dependent prefactor. For the case of our pUC19 model $N = 84$ and $\kappa = 5.0$, this prefactor is sufficiently close to unity (≈ 0.90) to be neglected in Figure 4 (main paper). The reduction in free-energy cost owes to semi-flexibility itself rather than simply a change in R_g: rescaling the flexible polymer into Kuhn beads with the same R_g gives results different from the semi-flexible case.

Dynamical simulations were performed with a standard coarse-grained, generic polymer methodology.[11] To model dsDNA, the width of the polymer is set to 5 nm and hence $\sigma = 5$ nm where σ is the bead size. Correspondingly, the Kuhn length is set to $L_{\mathrm{K}} = 20\sigma$ to match the 100 nm Kuhn length of dsDNA. The polymer is built out of 183 beads to give a contour length of 1047 nm in agreement with that of pUC19.

In correspondence with the theory, an ideal polymer was constructed in which there are no excluded volume interactions between monomers that are non-adjacent along the polymer backbone. Neighboring monomers are prevented from overlapping by the Weeks-Chandler-Anderson (WCA) potential which is a shifted and truncated Lennard-Jones interaction.[12] It is given by

$$U_{\mathrm{WCA}}(r) = \begin{cases} 4\epsilon \left[\left(\frac{\sigma}{r}\right)^{12} - \left(\frac{\sigma}{r}\right)^{6} \right] + \epsilon & \text{for } r < r_{\mathrm{c}} \\ 0 & \text{for } r \geq r_{\mathrm{c}} \end{cases} \tag{7}$$

where ϵ is the characteristic energy, here set to $k_{\mathrm{B}}T$, σ is the nominal monomer size, 5 nm, which is set in simulation units to 1, and r_{c} is the cut-off distance and is set to $2^{1/6}\sigma$.

Monomers along the polymer are bonded together via a Finitely Extensible Nonlinear Elastic (FENE) potential:

$$U_{\mathrm{FENE}}(r) = -\frac{1}{2}k_{\mathrm{f}}r_0^2 \ln\left(1 - \frac{r^2}{r_0^2}\right). \tag{8}$$

We follow the model of Kremer and Grest[13] and set $k_{\mathrm{f}} = 30\epsilon/\sigma^2$ and $r_0 = 1.5\sigma$. As we require a semi-flexible polymer, backbone stiffness is implemented via a harmonic potential given by

$$U_{\mathrm{bend}}(\theta) = \frac{1}{2}k_{\mathrm{s}}(\theta - \theta_0)^2 \tag{9}$$

where θ is the angle formed by three consecutive monomers along the polymer backbone, θ_0 is the equilibrium angle which is set to π, and k_{s} is the bending constant. For this potential, the Kuhn length is approximately equal to the bending constant: $L_{\mathrm{K}}/\sigma \approx 2k_{\mathrm{s}}/k_{\mathrm{B}}T$. As discussed above, we set $k_{\mathrm{s}} = 10k_{\mathrm{B}}T$ and thus have a Kuhn length $\approx 20\sigma$ in the simulations. The simulated polymer contained $N = 183$ monomers.

The confining walls are implemented as continuous surfaces. Interactions between the monomers and the walls are governed by the WCA potential as given above. Simulations are performed with the distance between the walls varying from $\tilde{h} = 2.5$–50.0σ. Due to the nature of the WCA interaction, the available space for the polymer will be $\sim \sigma$ less than this value. Likewise, as the theory corresponds to an infinitely thin polymer, the relevant height is this height minus the size of the simulation bead. Thus, the final simulation height used for plotting is $h = \tilde{h} - 2.0\sigma$.

As this work addresses static properties and not dynamics, hydrodynamics were not required in the simulations. For computational efficiency, we thus performed Langevin dynamics simulations in which the effects of the solvent are included implicitly in the equation of motion. This is achieved by adding a drag term and a random term to the standard molecular dynamics equation yielding

$$m\ddot{\vec{r}} = -\nabla U(\vec{r}) - \zeta\dot{\vec{r}} + \vec{R}(t). \tag{10}$$

In this equation, $U(\vec{r})$ is the sum of the conservative potentials, ζ is the friction coefficient, and $\vec{R}(t)$ is a random number that satisfies

$$\langle \vec{R}(t) \rangle = 0 \tag{11}$$

$$\langle \vec{R}(0) \cdot \vec{R}(t) \rangle = 2k_{\mathrm{B}}T\zeta\delta(t) \tag{12}$$

in accordance with the fluctuation dissipation theorem.

To obtain the confinement free energy from simulations, we followed the approach of Dimitrov *et al.*[14] by calculating the average force on the walls due to the monomers, $f_{\mathrm{conf}}(h)$. This is related to the confinement free energy by

$$f_{\mathrm{conf}}(h) = -\frac{d}{dh} G_{\mathrm{conf}}(h). \tag{13}$$

The free energy of confinement, G_{conf}, was calculated by numerically integrating the $f_{\mathrm{conf}}(h)$ data. Simulations were performed from very tight confinement up to $h/L_{\mathrm{K}} = 1.83$ and thus there is a numerical constant, G_0, that must be added to G_{conf}. This was calculated using the Chen-Sullivan formula to equal 0.100 $k_{\mathrm{B}}T$. The simulation results for G_{conf} are shown in Fig 4 (main paper) together with the Monte Carlo simulations from the main text (Fig. 3).

References

(1) Berard, D.; McFaul, C. M.; Leith, J. S.; Arsenault, A. K.; Michaud, F.; Leslie, S. R. Precision platform for convex lens-induced confinement microscopy. *Review of Scientific Instruments* **2013**, *84*, 103704.

(2) Kundukad, B.; Yan, J.; Doyle, P. S. Effect of YOYO-1 on the mechanical properties of DNA. *Soft matter* **2014**, *10*, 9721–9728.

(3) Odijk, T. Polyelectrolytes near the rod limit. *Journal of Polymer Science: Polymer*

Physics Edition **1977**, *15*, 477–483.

(4) Skolnick, J.; Fixman, M. Electrostatic persistence length of a wormlike polyelectrolyte. *Macromolecules* **1977**, *10*, 944–948.

(5) Dobrynin, A. V. Electrostatic persistence length of semiflexible and flexible polyelectrolytes. *Macromolecules* **2005**, *38*, 9304–9314.

(6) Manning, G. S. The persistence length of DNA is reached from the persistence length of its null isomer through an internal electrostatic stretching force. *Biophysical journal* **2006**, *91*, 3607–3616.

(7) Baumann, C. G.; Smith, S. B.; Bloomfield, V. A.; Bustamante, C. Ionic effects on the elasticity of single DNA molecules. *Proceedings of the National Academy of Sciences* **1997**, *94*, 6185–6190.

(8) Brunet, A.; Tardin, C.; Salomé, L.; Rousseau, P.; Destainville, N.; Manghi, M. Dependence of DNA persistence length on ionic strength of solutions with monovalent and divalent salts: A joint theory–experiment study. *Macromolecules* **2015**, *48*, 3641–3652.

(9) McFaul, C. M.; Leith, J.; Jia, B.; Michaud, F.; Arsenault, A.; Martin, A.; Berard, D.; Leslie, S. Single-molecule microscopy using tunable nanoscale confinement. SPIE NanoScience+ Engineering. 2013; pp 881102–881102.

(10) Sbalzarini, I. F.; Koumoutsakos, P. Feature point tracking and trajectory analysis for video imaging in cell biology. *Journal of structural biology* **2005**, *151*, 182–195.

(11) Slater, G. W.; Holm, C.; Chubynsky, M. V.; de Haan, H. W.; Dube, A.; Grass, K.; Hickey, O. A.; Kingsburry, C.; Sean, D.; Shendruk, T. N.; Slater, G. W. Modeling the separation of macromolecules: a review of current computer simulation methods. *Electrophoresis* **2009**, *30*, 792–818.

(12) Weeks, J. D.; Chandler, D.; Andersen, H. C. Role of repulsive forces in determining the equilibrium structure of simple liquids. *The Journal of chemical physics* **1971**, *54*, 5237–5247.

(13) Grest, G. S.; Kremer, K. Molecular dynamics simulation for polymers in the presence of a heat bath. *Physical Review A* **1986**, *33*, 3628.

(14) Dimitrov, D. I.; Milchev, A.; Binder, K.; Klushin, L. I.; Skvortsov, A. M. Universal properties of a single polymer chain in slit: Scaling versus molecular dynamics simulations. *The Journal of chemical physics* **2008**, *128*, 234902.

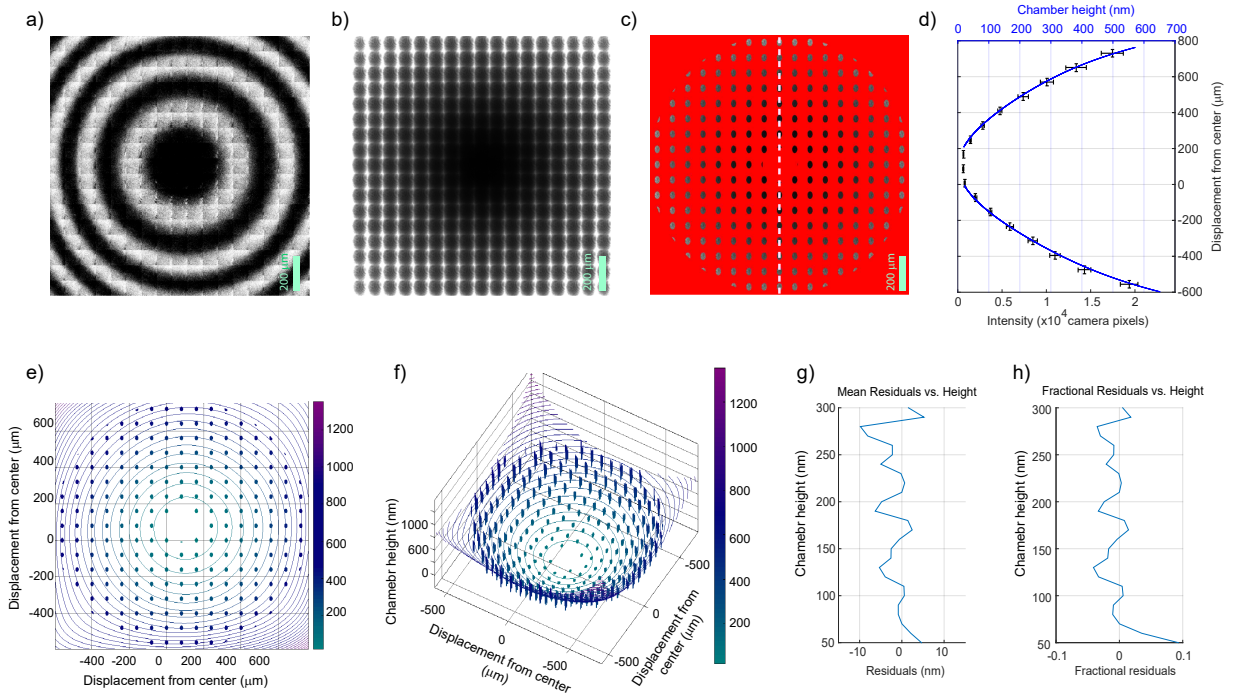

Figure S1: Chamber height characterization. The same y axis applies to panels **a** through **d**. **a)** Fringe scan: Stitched 17 × 17 raster scan of interference fringes caused by chamber geometry using 488-nm laser source. Exposure time = 50 ms; magnification = 90× (60× objective and 1.5× relay lens); total imaging region = 1360-μm square, step sizes = 80 μm, number of frames = 1. **b)** Dye scan: fluorescence of free Cy5 molecules in the chamber, with identical acquisition parameters as fringe scan, save for excitation with 647-nm laser; exposure time = 200 ms. **c)** Masked dye scan: Regions colored red are not used for the chamber height fit, eliminating the rasterization effect of the unmasked dye scan. The exclusion of regions of the chamber outside the doughnut-shaped area eliminates the center of the chamber, which, owing to coverslip-coverslip contact, deviates significantly from a polynomial curve, as well as the corners of the chamber, which are too dense with particles to be analyzed and thus an accurate determination of their height is not necessary. Dashed white line is the line along which the chamber height profile is shown in **d**. **d)** Chamber height profile: Solid blue line shows the fitted chamber height along the dashed white line in **c**. The central region of the chamber excluded from the fit is not shown. Black points and horizontal error bars show the mean and standard deviation in the normalized dye intensity for the parts of the fields of view along same dashed white line that are not masked out. Vertical error bars are the width of the non-masked out areas. Scaling the polynomial fit to absolute heights for this dataset was based on fixing the height to match two interferometry minima (innermost and second-innermost dark ring in **a**). Inset: Dye intensity at low chamber heights. **e,f)** Plots of dye intensity (solid surface plot) and fitted chamber contours (lines) from different viewing angles (directly above, and tilted, respectively). **g,h)** Mean residuals in (absolute and proportional) of the fitted height, in 10-nm height bins.

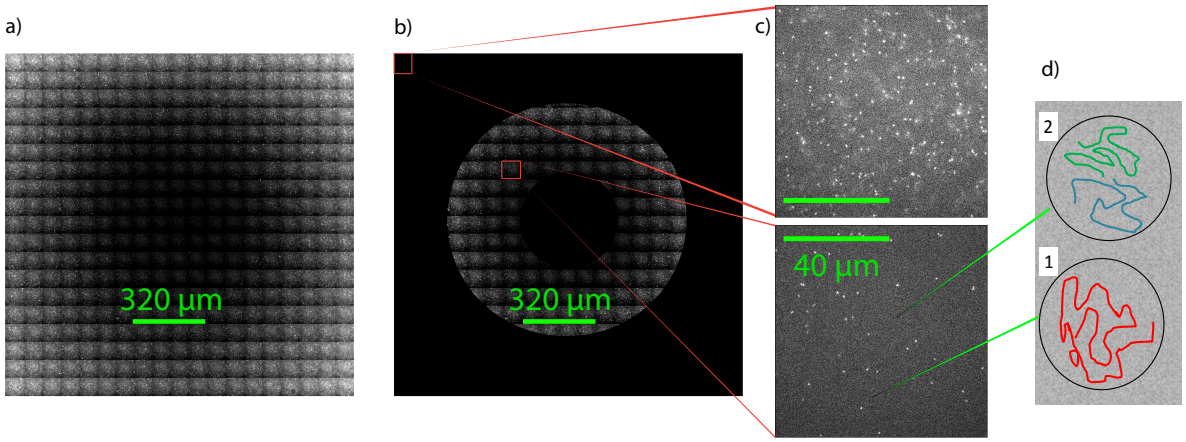

Figure S2: **a)** DNA scan: Stitched 19 × 19 raster scan of the fluorescence of freely diffusing DNA molecules. The images were taken using a 488-nm laser source to excite the YOYO-1 DNA stain. This scan was performed with the following settings: Camera magnification = 90, step sizes = 80 μm, number of frames = 50. **b)** Masked DNA scan. A 'doughnut'-shaped mask was used to select regions of the full scan that can be used for tracking molecules. The center is masked out because there were no molecules to track at the center, while the peripheral area is masked out because the chamber height in that area is significantly greater than our optical system's depth of field, and thus molecules can appear blurry and are not tracked reliably. **c)** Selected fields of view from the stitched scan, to compare the "trackable" region to the region where particles are not reliably in focus. **d)** Schematics of typical particle trajectories obtained from the particle tracking algorithms.

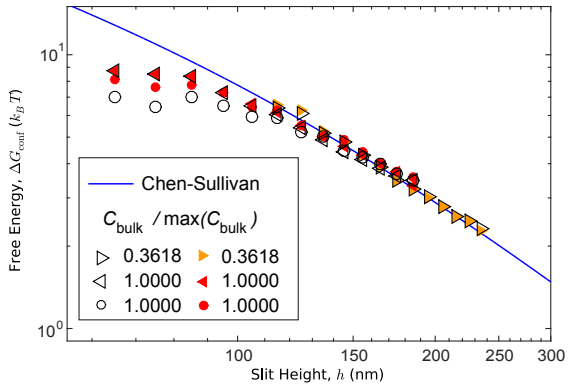

Figure S3: ΔG_{conf} versus h, showing the effects of the alternative chamber-fitting technique. Colored markers show measured ΔG_{conf} for the three highest-concentration datasets, using the technique of scaling the polynomial fit of the measured dye intensity based on the two innermost interferometry minima. Uncolored open markers show ΔG_{conf} using one interferometry minimum and fixing the height at the position in the chamber corresponding to the polynomial fit's minimum.